Journal of Materials Chemistry A

Mechanical and electrical changes in electrochemically active polyimide binder for Li-ion batteries

Journal:	*Journal of Materials Chemistry A*
Manuscript ID	TA-ART-09-2024-006671.R1
Article Type:	Paper
Date Submitted by the Author:	27-Nov-2024
Complete List of Authors:	Huey, Zoey; National Renewable Energy Laboratory, Materials, Chemical, and Computational Science Directorate; Colorado School of Mines, Department of Mechanical Engineering Quinn, Joseph; Pacific Northwest National Laboratory Rodrigues, Marco ; Argonne National Laboratory, Chemical Sciences and Engineering Division Rajendran, Sathish; Argonne National Laboratory Wang, Chongmin; Pacific Northwest National laboratory, Environmental Molecular Sciences Laboratory DeCaluwe, Steven; Colorado School of Mines, Mechanical Engineering Jiang, Chunsheng; National Renewable Energy Laboratory, Materials, Chemical, and Computational Science Directorate

Mechanical and electrical changes in electrochemically active polyimide binder for Li-ion batteries

Zoey Huey[a,b], Joseph Quinn[c], Marco-T. F. Rodrigues[d], Sathish Rajendran[d], Chongmin Wang[c], Steven DeCaluwe[b], and Chun-Sheng Jiang[a,*]

[a] Materials, Chemical, and Computational Science Directorate, National Renewable Energy Laboratory, Golden, Colorado 80401, United States

[b] Department of Mechanical Engineering, Colorado School of Mines, Golden, Colorado 80401, United States

[c] Environmental Molecular Sciences Laboratory, Pacific Northwest National Laboratory, 902 Battelle Blvd, Richland, WA 99354, United States

[d] Chemical Sciences and Engineering Division, Argonne National Laboratory, Lemont, IL, USA

*Email: chun.sheng.jiang@nrel.gov

Key words: Polyimide binder; Li ion battery; Microscale mechanical mapping; Scanning transmission electron microscopy; Scanning spreading resistance microscopy.

Abstract

Polyimide binders are often used in electrodes made with silicon for lithium-ion batteries for their mechanical strength and adhesion, which help mitigate mechanical issues with large volumetric expansion. These binders can be electrochemically active, but it is difficult to characterize what physical and chemical changes occur due a composite electrode with multiple components and processes at play. In this work, we study electrodes consisting only of polyimide binder and conductive carbon, using scanning probe-based techniques— contact resonance, force volume, and scanning spreading resistance microscopy—along with cryo-scanning transmission electron microscopy, electron energy loss spectroscopy, and energy dispersive x-ray

spectroscopy. We show that lithium becomes trapped in the binder during cycling and results in large initial capacity losses, the formation of dendrite-like features, column-like domains of significantly increased mechanical modulus, and a slight increase in electronic resistivity.

1. Introduction

As the renewable energy transition and the electric vehicle industry gain momentum, lithium-ion batteries (LIBs) are in higher demand than ever, necessitating improved performance [1]. Composite electrodes, made of active material particles and other additives held together with a binder, are prevalent due to their ease of manufacturing and the ability to combine constituent material properties for improved average electrode properties [2]. While the active materials provide the bulk of the capacity, the other components, such as the binder, play key roles as well. Binder behavior and properties may change during cycling, potentially impacting active material performance and utilization.

Polyimides (PIs) have been proposed as binders for LIB electrodes made with silicon (Si) and other materials due to their mechanical strength and stability at high temperatures, allowing for higher loadings, increases in capacity, and improved long term cycling when compared to other binders such as polyvinylidene fluoride (PVDF) [3–8]. Improved mechanical robustness is particularly beneficial in an electrode such as Si, where mechanical damage frequently results from repeated volumetric expansion and contraction during lithiation and delithiation [6,9]. PI binders have demonstrated good adhesion to current collectors, mitigating issues with delamination due to Si expansion and contraction [5].

The specific role of polyimide binders within a composite electrode system is not well understood, as it can be challenging to characterize and disentangle the contributions of any individual electrode component [10]. Additionally, evidence suggests that certain aromatic PI

binders are electrochemically active, possessing lithiation capacity without any active material [11,12]. It is important to elucidate any individual component effects, such as polyimide binder, as its use for one property, such as mechanical strength, may have unintended effects in other areas and result in drawbacks. To optimize PI-containing composite electrode design, a quantitative understanding of the material function and evolution during battery cycling is required.

This work aims to understand how an aromatic polyimide binder changes during cycling to contribute to a more complete understanding of its use in composite electrodes. We present electrochemical data from electrodes made with only PI binder and conductive carbon, showing high first cycle capacity losses and large voltage hysteresis as well as a set of correlative characterizations. We discuss scanning probe-based mechanical measurements, contact resonance (CR) and force volume (FV), that show the formation of column-like structures with increased modulus after both first cycle lithiation and delithiation extending from electrode surface to current collector. These measurements are complemented by cryo-scanning transmission electron microscopy (STEM) images, electron energy loss spectroscopy (EELS), and energy dispersive x-ray spectroscopy (EDS) that show significant morphology changes after cycling, forming a porous dendrite-like structure. Lithium and lithium compounds are observed within the dendritic features after both lithiation and delithiation. Lastly, we present scanning spreading resistance microscopy (SSRM) data that shows a uniform and consistent distribution of carbon particles and binder and an increase in resistivity after delithiation.

2. Experimental Details

2.2 Electrode fabrication

The PI/C45 electrodes were fabricated with a 20 wt% solution of Ensinger P84 polyimide binder (PI) in N-methyl pyrrolidone (NMP; Sigma Aldrich), prepared by homogenizing the polymer and solvent in a rotary mixer for 24 h at 50–75 rpm. The reported structure of this PI is described elsewhere [5,11]. This solution was combined with C-45 conducting carbon (Timcal) to form a viscous slurry, containing a 75:25 PI:C45 mass ratio. Additional NMP was added until the desired viscosity was achieved. The slurry was homogenized in a Thinky mixer at 2000 rpm for 4 min and 2200 rpm for 30 s, and then coated on a copper foil using the doctor blade method. The electrode was dried overnight at 75 °C, and further cured at 350 °C under vacuum for 1 h. The final thickness was 10-13 μm.

2.2 Electrochemical cycling

Electrodes were tested in half cells (2032 format), using Li metal counter electrodes and Celgard 2500 separators. The electrolyte was 1.2M $LiPF_6$ dissolved in 3:7 wt ethylene carbonate:ethyl methyl carbonate. 40 μL of electrolyte was added to the cell, in large excess of the total pore volume present in cell components. Cells were cycled at C/5 between 5 mV and 2 V, with a voltage hold at each cutoff until the current decayed to C/50. Specific capacity values are reported based on the combined weight of both the PI and C45, calculated assuming only the PI contributes to capacity and has a theoretical reversible capacity of 600 mAh/g [11]. 1C current was assumed to be ~450 mA g^{-1}. The lithiated sample underwent one discharge and the delithiated sample underwent one discharge and one charge.

2.3 Contact Resonance-Force Volume

Sample cross sections were made by sandwiching electrode samples between silicon wafers with EpoTek conductive epoxy. The cross sectional samples were mechanically polished

using diamond lapping film down to 0.5 μm in dry conditions in Ar glovebox, and then by a JEOL cooling cross section polisher (JEOL CCP) with an air-free transfer chamber under an argon ion beam with 5 kV energy and ~150 μA current.

CR and FV measurements were taken with a Bruker Dimension Icon AFM in PeakForce QNM+CR mode and Bruker DDLTESP probes (nominal spring constant k=95 N/m). The AFM was installed in an Ar-filled glovebox to prevent air exposure. CR and FV data were processed in Bruker Nanoscope software. Additional information on the principles of CR and FV can be found in the Supplemental Information.

2.4 STEM-EELS and -EDS

Lithiated and delithiated samples were moved to a Thermo Scientific Helios Hydra 5 plasma-focused ion beam-scanning electron microscope (PFIB-SEM) using a QuickLoader Load Lock, which kept them in an atmosphere free environment during the transfer process. The PFIB-SEM was used to create lamellae of each sample for cross-sectional cryo-STEM imaging. The samples were then transferred to a 300kV monochromated FEI Titan TEM with a probe aberration corrector using a Gatan cryo-transfer station to prevent atmosphere exposure. The cryo-holder was a Gatan Elsa Holder model 698. HAADF imaging was performed with an electron dose rate of ~$4.5x10^7$-$2x10^8$ $e \cdot Å^{-2} \cdot s^{-1}$. For cryo-EELS characterization a Gatan Image Filter Quantum Spectrometer was used. The pixel width, dispersion, and exposure time were 3-5nm, 0.05eV/ch, and 0.05s respectively. The energy resolution for each spectrum was close to 1eV. Spectra of the Li K-edge were analyzed using a Hartree-Slater cross sectional model, a power law background model, and were corrected for plural scattering. Cryo-EDS analysis was characterized with an Oxford Instruments Aztec X-Max detector.

2.5 SEM

SEM data was collected with a Hitachi S-4800 SEM using an accelerating voltage of 9 kV. The EDS was collected on the same instrument using a Thermo Fisher Pathfinder EDX detector and the same accelerating voltage.

2.6 SSRM

SSRM measurements were collected with the same AFM as the CR-FV data using a Bruker SSRM module. Bruker DDESP-V2 conductive diamond-coated Si probes were used in AFM contact mode with a bias voltage of -0.25 V applied to the sample, while the probe was floating grounded. The data was processed using Bruker Nanoscope and Gwyddion software packages.

3. Results

3.1 Electrochemical characterization

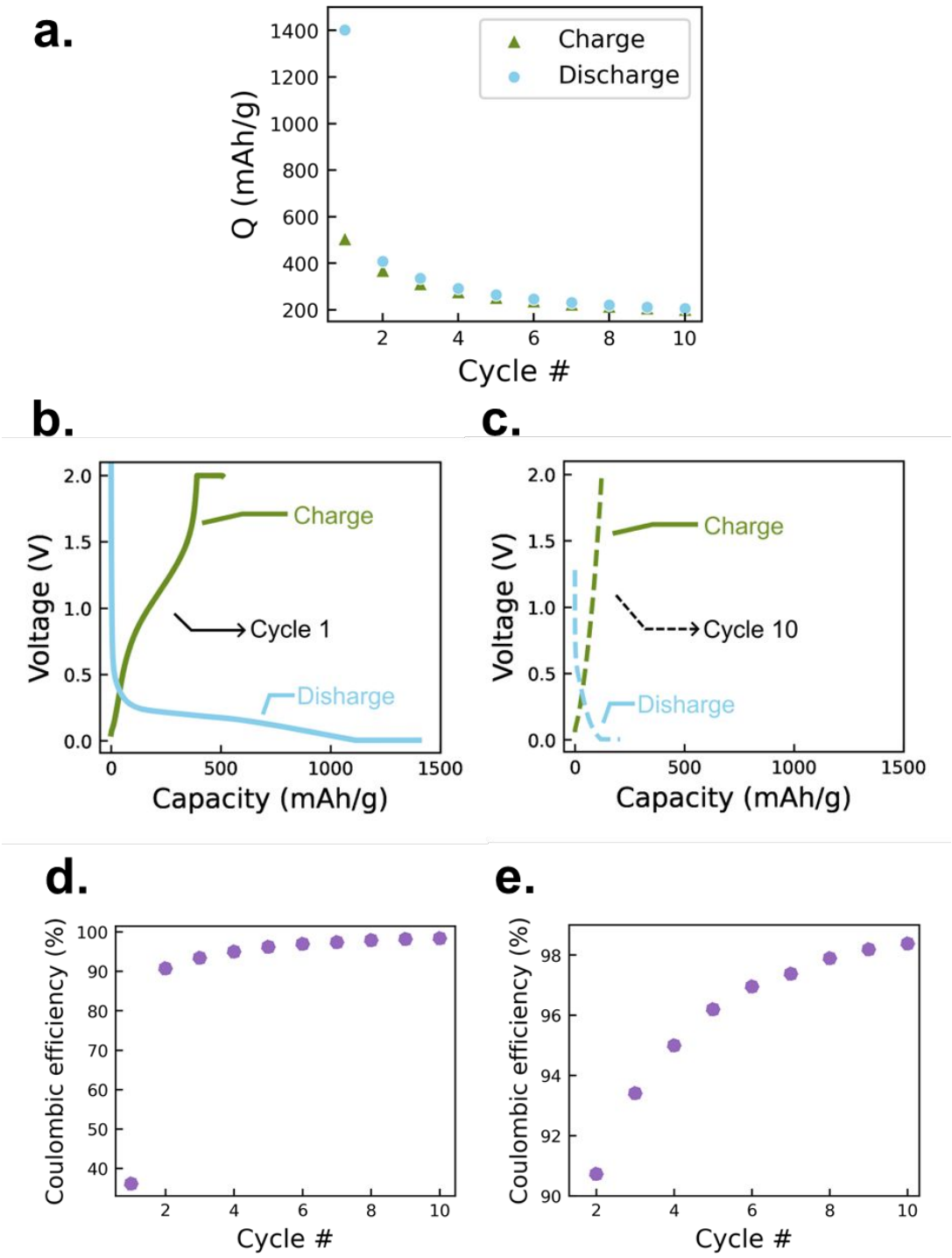

Figure 1: Electrochemical cycling data for PI/C45 electrodes showing a) capacity over 10 cycles, b) 1st and c) 10th voltage profiles, d) Coulombic efficiency over 10 cycles and e) Coulombic efficiency over 10 cycles with a modified y-axis to better visualize later efficiencies. Capacities are calculated for combined PI and C45 mass.

Electrochemical cycling data of PI/C45 electrodes with no active material over 10 cycles shows a relatively large initial lithiation capacity of 1402 mAh g_{PI+C45}^{-1} after a voltage hold, due to slow kinetics (Figure 1a), with significant irreversible first cycle capacity loss: the initial delithiation capacity was 506 mAh g_{PI+C45}^{-1}, resulting in an initial coulombic efficiency (CE) of 36.1% (Figure 1d). After the first cycle, the coulombic efficiency improves somewhat, with a second cycle CE of 90.7% and a 10^{th} cycle CE of 98.4%, but capacity loss persists throughout cycling. It should be noted that this cycling is generally poor, as the electrodes contain no active material. As the binder content for standard composite electrodes is typically less than 10 wt%, its impact on overall CE should be much less significant due to active materials in the composite electrode being the main player for lithiation/delithiation. The first cycle voltage profile shows significant separation between discharge and charge, suggesting that Li remains irreversibly trapped in the electrode after delithiation. Experiments reported elsewhere using electrodes where the PI was the sole active component found initial delithiation capacities as high as ~1000 mAh g_{PI}^{-1}, indicating that contributions of C45 to the capacities shown above are relatively small [11].

3.2 CR-FV

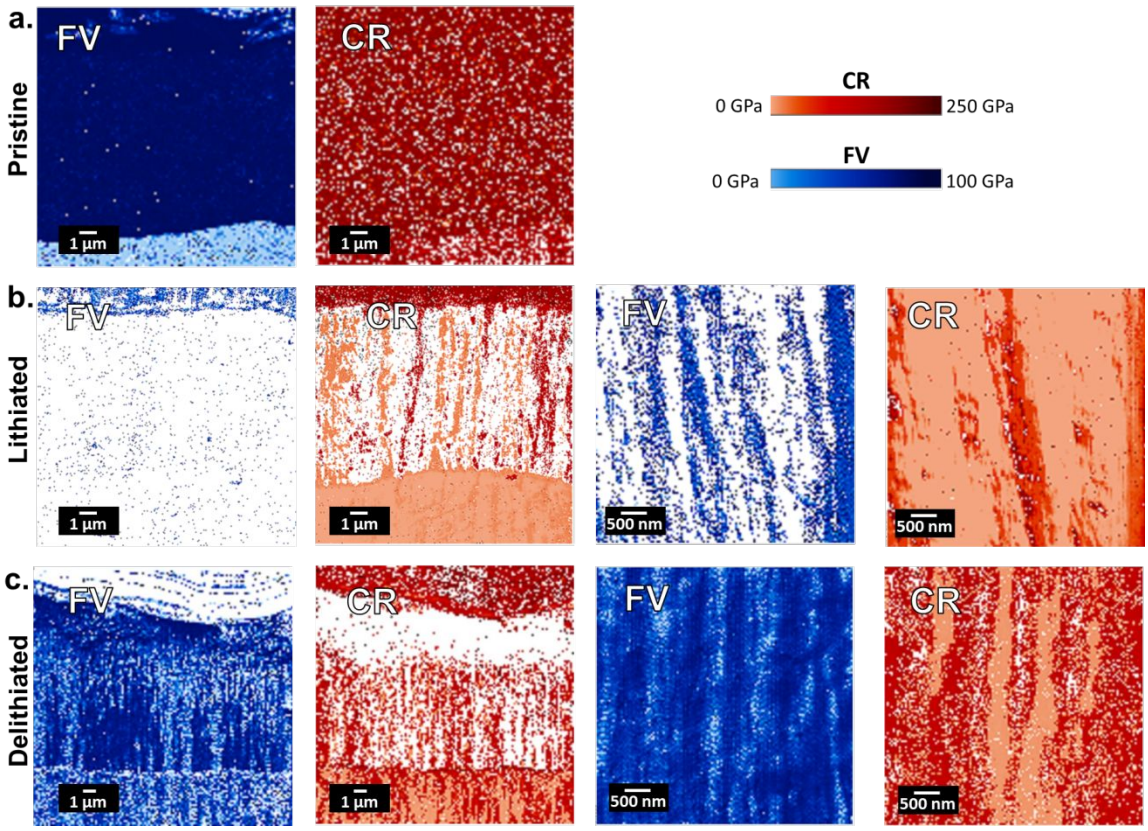

Figure 2: Representative cross section CR-FV maps of a) pristine, b) first cycle lithiation and c) first cycle delithiation of PI/C45 electrodes. Pristine electrodes show spatially homogeneous, low-modulus materials, whereas cycled electrodes (both lithiated and delithiated) show domains of high modulus that extend from current collector to the electrode surface. White pixels correspond to points where data could not be collected due to a modulus that was out of range for the technique or an artefact on the sample surface. Corresponding height maps for all images can be found in Figure S1.

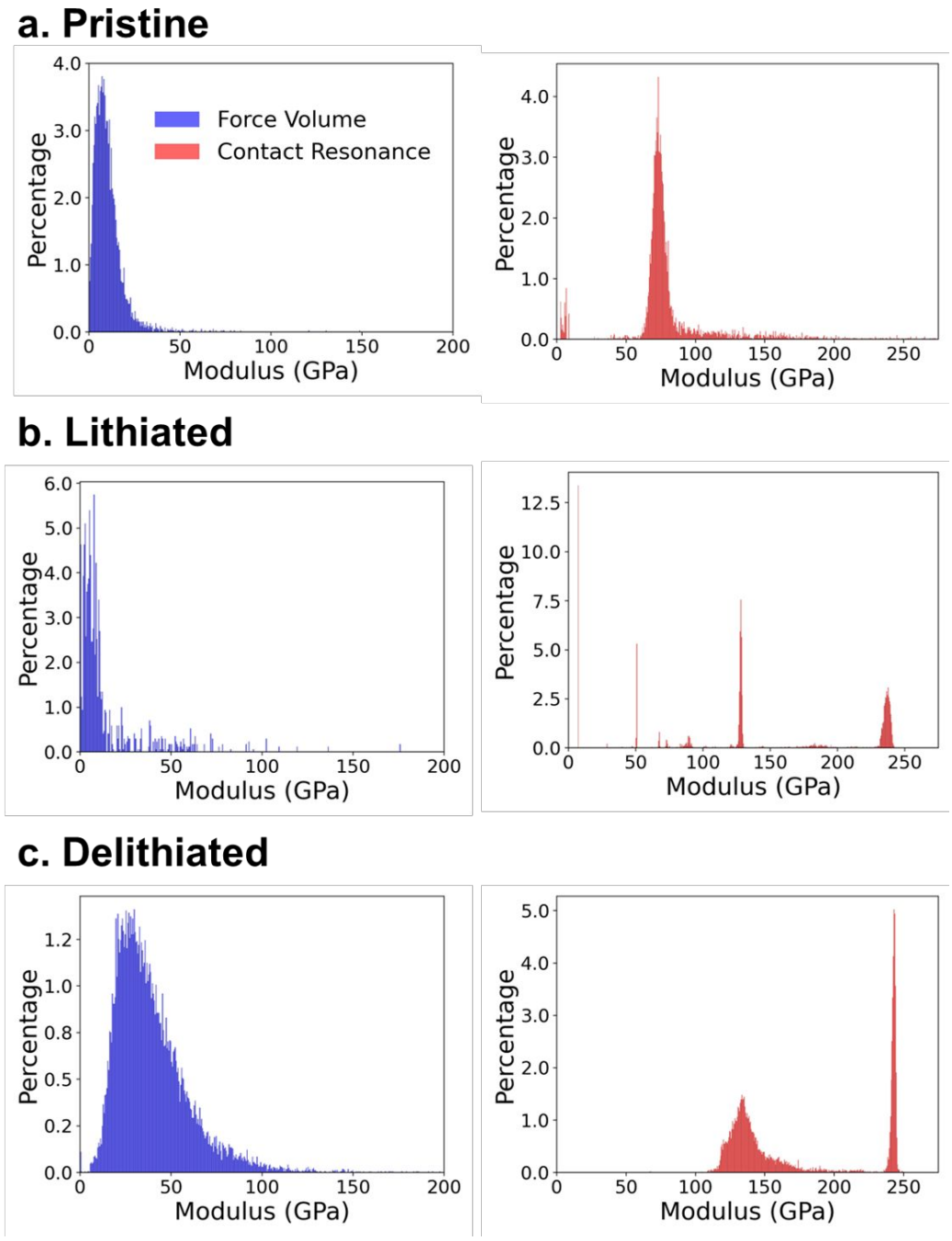

Figure 3: Representative histogram data for CR and FV maps for a) pristine, b) lithiated, and c) delithiated electrodes. The CR data for the lithiated and delithiated sample show two distinct peaks, whereas pristine electrodes have one main peak. The modulus tends to increase in cycled electrodes, relative to pristine electrodes. Bin widths are 0.5 GPa and bar heights sum to 100.

CR and FV were used to image cross sections of the pristine, lithiated, and delithiated electrodes. These measurements provide microscale maps with sub-micron depth sensitivity of

mechanical modulus. CR is better suited for higher modulus materials and FV is better for lower modulus materials; in tandem, they can fully characterize the range of electrode materials present [13]. It should be noted that these measurements, particularly CR, require precise probe calibration and flat surfaces to give quantitative results [14–16]. While these measurements were conducted with the same calibrated probe and instrument parameters to maintain consistency across the sample set, and the samples were polished to provide as flat a surface as possible by ion-milling, composite electrodes have unavoidable roughness (~ 20 nm, Figure S2) due to porosity and individual particles, and the constituents in the composites vary in wide mechanical ranges. As such, these results should be seen as qualitative, with relative values and spatial modulus distribution providing useful information.

The pristine electrode FV map (Figure 2a) shows a low and uniform modulus throughout the cross section. PI binder only samples (i.e. with no conductive carbon) were measured (Figure S3) and also showed a low modulus, indicating that the pristine modulus of the PI/C45 electrode is primarily impacted by the PI. This is consistent with low modulus values reported by binder manufacturers, around 3.5-4 GPa [17,18]. The CR data for the pristine electrode shows the same uniformity, but a higher measured modulus. This may be due to sample roughness or calibration error. Additional histograms for all samples can be found in Figure S4, but do not deviate significantly from the trends shown herein.

Lithiated electrode maps (Figure 2b) show a significant shift in mechanical properties, relative to the pristine electrode samples. The FV maps have a large amount of white space, indicating that little FV data could be collected, which typically corresponds to a higher modulus material [19]. The CR maps show domains two distinct moduli: one around 120 GPa and another around 240 GPa (Figure 3b), whereas the pristine electrode CR map has a single, broad peak

centered at roughly 75 GPa. From Figure 2, these high-modulus domains have a column-like morphology, extending from the current collector to the electrode surface. The column features are roughly 500 nm to several μm wide and the higher modulus domain area is significantly larger than that of the lower modulus.

The delithiated electrode CR results (Figure 2c) showed a similar morphology as the lithiated sample, with columns of high and low modulus domains extending through the electrode thickness. The relative modulus values of the high and low domains are very similar to those observed in the lithiated electrode, but there is more low modulus area than the high modulus area, the opposite of the lithiated electrode. The FV maps appear to show a similar column morphology, but the histograms do not show any distinct domains, likely because it was unable to detect the higher modulus area (Figure 3c). The peaks in the delithiated FV histogram are broader than for the other maps, with a full width half maximum (FWHM) of 37.7 GPa, as compared to pristine and lithiated FWHMs of 7.8. and 14.8 GPa, respectively. This distribution indicates a wider range of modulus values.

We also collected mechanical data on the electrode surface (Figure S5). Like the cross-sections, the resulting maps scattered domains of high and low modulus on lithiated and delithiated samples, consistent with imaging perpendicular to the columnar structures. However, as previous discussed, sample smoothness is critical for the CR-FV measurements, and the electrode surfaces are significantly rougher than the polished cross sections (Figure S2c). For this reason, the modulus values measured on the surface are less reliable. Additionally, the surface morphology is smoother for the lithiated sample than the pristine and delithiated samples (Fig. S2c), making comparisons across the sample set challenging.

3.3 STEM-EELS and -EDS

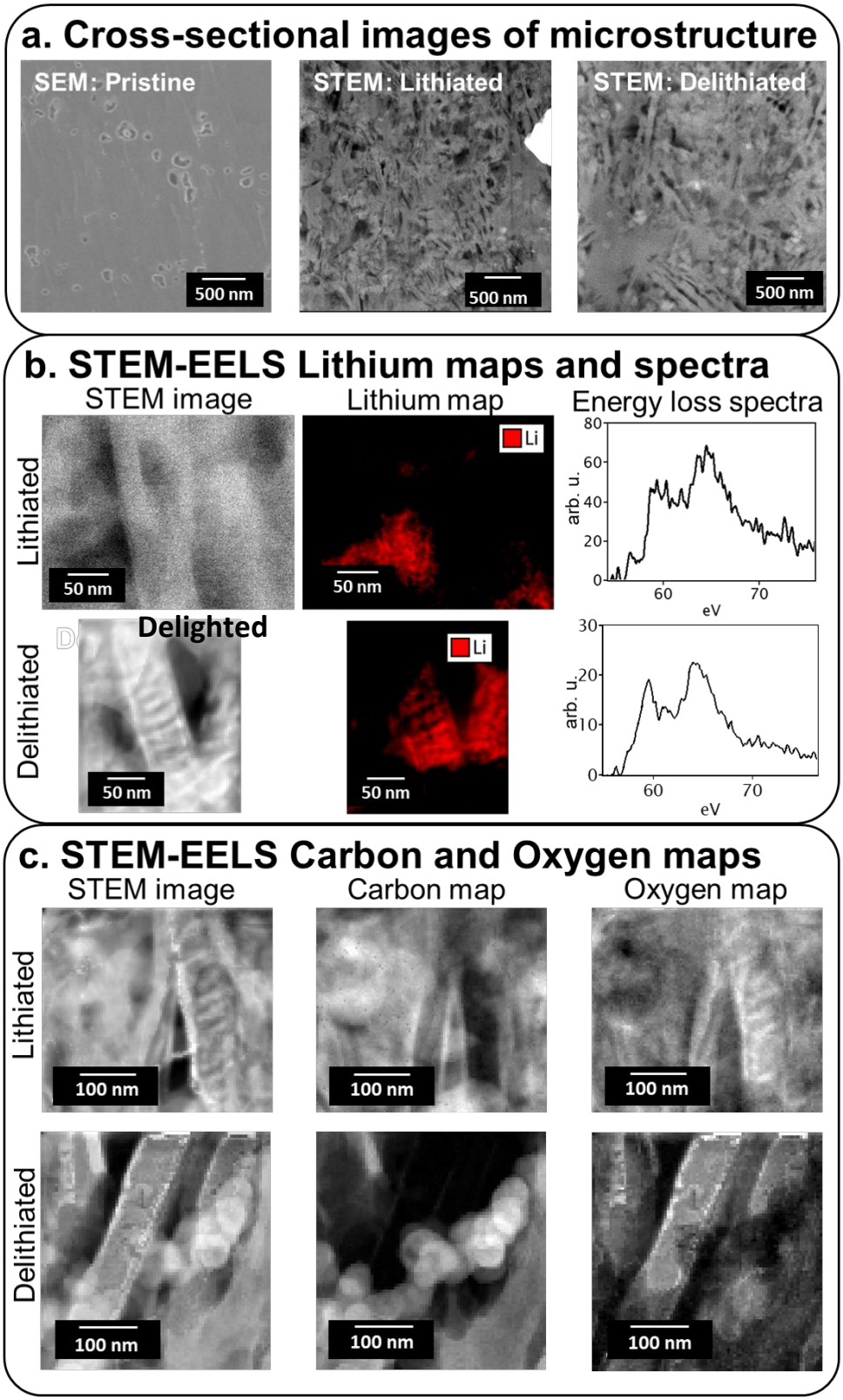

Figure 4: a) Cross sectional SEM of pristine electrode showing solid and non-porous structure and cross sectional STEM of lithiated and delithiated electrodes showing dendritic structure. b) STEM-EELS data showing Li elemental map and energy loss spectra for lithiated and delithiated samples. (c) STEM and EELS maps of carbon and oxygen of lithiated and delithiated electrodes.

Cross section imaging was also conducted with SEM and STEM, and elemental mapping was done using EDS and EELS (Figure 4). The SEM image (Figure 4a) of the pristine sample shows a dense solid electrode with low porosity and the individual C45 particles cannot be distinguished. STEM images of the lithiated and delithiated samples show a significant morphology change, with an increase in porosity and formation of dendrite-shaped features (Figure 4a). These features are roughly vertically oriented perpendicular to the electrode surface and are approximately 100 nm across. The delithiated sample has more smooth areas and fewer dendrite-like features than the lithiated sample, but many of the same features are still observed. Additional STEM-EELS images of different locations showing similar features can be found in Figure S6.

In the lithiated electrode STEM-EELS mapping (Figure 4b), Li is observed mainly in the dendrite-like features, although they do not appear to be entirely made of Li and should not be confused with Li dendrites. The energy loss near edge fine structure (ELNES), as shown in the right panels of Fig. 4(b), indicates the presence of both Li metal (a shoulder at approximately 55 eV) and Li_2O (two peaks at approximately 59 and 65 eV) (reference spectra can be found in Figure S7). The delithiated electrode also has Li confined to the dendrite structures, with the Li_2O signal being stronger than Li, indicating more Li_2O than Li.

STEM-EELS mapping of the lithiated sample focused on carbon and oxygen (Figure 4c) shows carbon located throughout the electrode, except in oxygen-rich areas that appear to correspond to the dendrite-like structures where the Li was also observed, although the features in the lithiated sample are more difficult to distinguish. In the delithiated sample, however,

individual round carbon areas, corresponding to the C45 particles, are clearly seen, as well as the dendritic structures where the oxygen is located. A small amount of fluorine is observed and scattered throughout both samples (Figure S6), which likely came from the electrolyte and is indicative of solid electrolyte interphase (SEI).

STEM-EDS shows relatively homogeneous distribution of carbon and oxygen in all three samples (Figure S8). It should be noted, however, that the EDS interaction depth (~µm) is larger than the average C45 particle size (~100 nm) as well as the dendritic features (~100 nm), so heterogeneity at a smaller scale cannot be detected with this technique.

3.4 SSRM

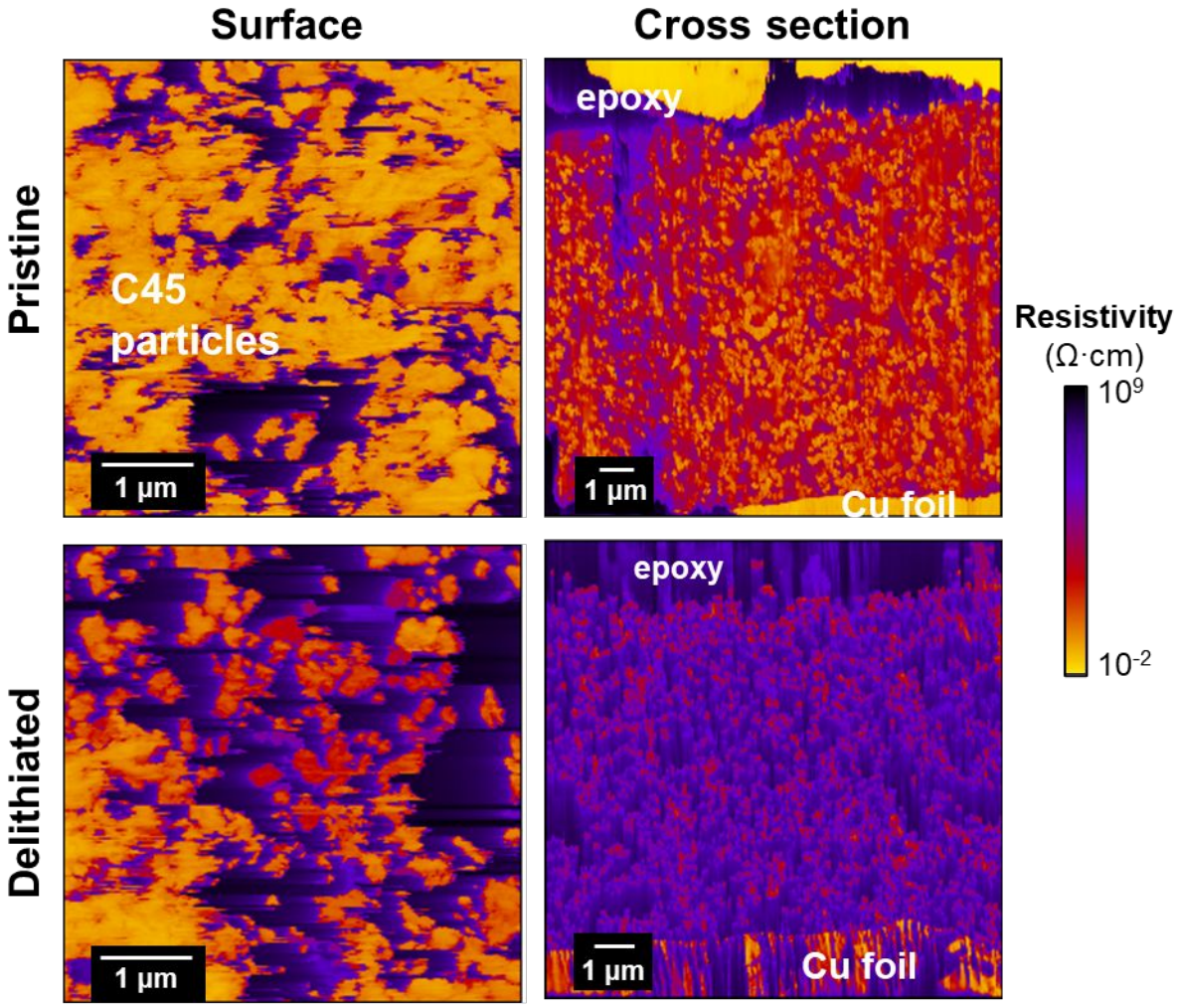

Figure 5: Surface and cross sectional SSRM resistivity maps for the pristine and delithiated electrode showing low resistivity C45 surrounded by a high resistivity PI matrix. The delithiated samples is more resistive overall than the pristine sample. Corresponding height maps can be found in Figure S9. It should be noted that the scan size on the sample surface is limited by roughness, resulting in a discrepancy in scaling between surface and cross section maps.

Both surface and cross-sectional resistivity maps were collected via SSRM (Figure 5), providing <100 nm scale spatial electronic resistivity with a depth sensitivity on the order of 30-50 nm, providing highly localized resistivity measurements of electrode components. The pristine electrode maps clearly show both individual and clusters of low resistivity C45 particles surrounded by a matrix high resistivity PI binder, which is consistent with previous SSRM work [20]. The C45 particles are uniformly distributed throughout electrode thickness and across the surface. Cross sections of PI-only coated on copper current collector were also measured as a reference (Figure S10) and found to have a high resistivity (~10^7 Ω• cm). Curing, which has been found to improve performance in electrodes made of Si active material, carbon, and PI, had minimal impact on PI resistivity [11,21].

After delithiation, an increase in resistivity was observed, particularly in the cross sectional maps, which is consistent with other SSRM measurements of cycled electrodes [10,22]. The individual lower resistivity carbon particles were still observed and still distributed similarly to the pristine electrode. SEI components are highly resistive, which contributes to this increase in resistivity [22,23]. The fluorine observed in the STEM-EELS data also indicates that SEI was formed on these samples. Additionally, the Li_2O observed may also contribute to the increase in resistivity [23,24]. The resistivity distribution is like that in the pristine electrode and there are no distinct morphologies matching the CR-FV and STEM data.

The lithiated sample could not be measured with SSRM, as the surface became unstable during scanning and consistent contact with the probe tip could not be maintained. This

instability is likely due to the large amount of Li present in the sample that moved when the bias voltage was applied.

4. Discussion

The characterization presented here indicates that significant and irreversible morphological, chemical, and structural changes occur in the PI/C45 electrodes because of cycling, resulting in poor electrochemical performance and changes in mechanical properties. A large irreversible first cycle capacity loss indicates that the Li storage mechanism is irreversible, or that immediate and significant transformation severely limits capacity, and any subsequent Li storage is inhibited. Electron microscopy (EM) images show that a porous microstructure with dendrite-like features develops after both lithiation and delithiation, as compared to a uniformly dense cross section in the pristine electrode. CR-FV mechanical maps show a homogenous and low modulus in the pristine sample, but column-like domains of high modulus in large amounts in the lithiated sample, and in smaller amounts in the delithiated sample.

These irreversible changes are accompanied by evidence that lithium becomes trapped in the electrode and remains after delithiation. STEM-EELS shows evidence of lithium in both cycled samples, in the form of Li metal and Li_2O in the lithiated sample and Li_2O only in the delithiated sample. This is consistent with the capacity loss shown in the electrochemical data. The Li map shows partially overlap of Li content with the dendrite-like structure, but not fully consistent with the dendrite structure (Fig. 4b). The presence of lithium is also correlated to the mechanical changes in the PI/C45 electrodes. The pristine electrode showed a uniformly low modulus, while the lithiated sample had a larger amount of high modulus area, and a smaller amount of lower modulus domain, where the FV values were similar to the pristine sample. The delithiated sample had a smaller amount of the high modulus area, with a similar modulus to the high modulus area in the lithiated sample. The FV results for the delithiated sample showed a higher

average modulus than the pristine and the lithiated, as well as a greater range of values. These results suggest that the lowest modulus domain corresponds to non-lithiated binder, and the high modulus domain corresponds to lithiated binder. Delithiated material is not immediately obvious in the CR-FV results, but it likely has a modulus that is greater than that of non-lithiated material, but not so much greater that it has a distinct histogram peak; this is supported by the more dispersed FV results for the delithiated sample. The dendrite structure is ~100 nm wide, as shown in STEM-EELS maps, whereas the lithiated/delithiated domain width in the CR-FV maps is much larger, on the order of one micron. This difference may be caused by insufficient spatial resolution of the mechanical mapping, where the mechanical map is a result of the average over the local dendrite and surrounding areas. The EM images show overall porous structures surrounding the dendrite-like structure, indicating the lithiation/delithiation process also affects the structure of surrounding area in addition to the dendrites. It is possible that nano-scale porosity, near or below the interaction depth of CR-FV (<500 nm) [25,26], impacts the measured modulus values. However, quantitative measurements of such small pores are challenging and more study is required to determine the exact relationship between porosity and CR-FV mechanical modulus.

Several mechanisms have been proposed in the literature for lithium storage in polymeric materials [11]. These include electrochemical doping [27], redox reactions within conjugated aromatic polymers [28,29], and the decomposition of the polymer into a hydrogen-containing carbon network, as proposed by Obrovac et al [12,30]. It is not clear which mechanism is responsible for Li storage in this PI binder [11], and how the dendrite-like structure was created during lithiation and remained after delithiation. The results presented here do not definitively point to a specific theory. Polymer doping would increase charge carrier density, implying a

decrease in resistivity, but a slight overall increase in resistivity was observed with SSRM [27]. Additionally, the large capacity loss observed indicates that the amount of Li stored is greater than possible through redox chemistry alone. The polymer decomposition theory also suggests a decrease in resistivity, due to the formation of more conductive carbon, which is not observed in these samples. However, this theory may explain the high modulus domains observed with CR-FV. While the mechanical properties of carbon can vary greatly depending on various factors, it generally has a higher modulus than that measured in the pristine and PI-only samples [31,32]. Additionally, the proposed decomposition reactions include Li_2O as a product, which was observed in both the lithiated and delithiated samples.

There are several possible sources for the formation of the Li_2O that was observed in both the lithiated and delithiated samples. It should be noted that one possible source of Li_2O is air exposure, as Li is highly sensitive to oxidation [33]. All samples were prepared in air-free Ar gloveboxes and transferred in airtight containers, but minor air exposure is always a possibility during transfer. However, the evidence of Li metal in the lithiated sample indicates that any air exposure was limited, as not all the Li reacted. As previously mentioned, Li_2O is a product in the polymer decomposition mechanism proposed and is also a known inorganic SEI product [12,23].

Although further study is required to better understand the Li storage mechanism in this PI binder, the changes that occur during the PI binder lithiation have potential impacts beyond added benefits of improved adhesion. The irreversible first cycle losses of the binder may contribute to initial losses in electrodes, such as Si anode, which already suffer from irreversible capacity losses from SEI formation [34]. The non-uniform mechanical changes may result in unexpected behavior, such as areas of increased weakness that are preferentially damaged during cycling and become mechanical failure points [35]. A complete understanding of mechanical

behavior is crucial in a system such Si, which is plagued by mechanical issues, and for which PI binder is specifically used for mechanical benefits.

5. Conclusion

This work analyzes electrodes consisting solely of PI binder and conductive carbon to understand the physical and chemical changes occurring when the binder electrochemically lithiates and delithiates. PI is of increasing interest as a binder in composite electrodes in research settings, particularly for systems such as Si, and as such it is critical to directly evaluate the electrochemical and mechanical properties during battery cycling. Results show that these binder/carbon additive electrodes have a high initial capacity but undergo large initial capacity losses during the first cycle and afterward. CR-FV mechanical mapping showed uniform pristine samples with a low modulus, but column-like domains extending from surface to current collector with a higher modulus that form during lithiation and remain even after subsequent delithiation. A greater fraction of the electrode consists of the high modulus domain in the lithiated sample. This high modulus domain likely corresponds to lithiated material that has undergone an irreversible structural change. STEM-EELS and EDS showed a solid, low porosity pristine electrode and the formation of dendrite-like structures in the lithiated and delithiated samples. Lithium was found in both samples, in the form of Li metal and Li_2O in the lithiated sample and Li_2O only in the delithiated sample, and it appeared to be confined to the dendritic structures. SSRM resistivity mapping showed uniformly distributed C45 particles through the electrode cross section and a slight increase in resistivity in the delithiated sample compared to the pristine sample. This work suggests that these physical changes may occur in any electrodes made with this material, resulting in unintended effects such as capacity loss and mechanical failure during cycling that are difficult to disentangle from other research approaches. Other types of polyimide, with different mechanical, physical, and electrochemical behaviors, are

becoming increasingly popular in battery research [4], and their individual contributions should be similarly analyzed to better understand the impacts of their use on overall electrode performance.

Acknowledgements

This work was authored in part by the National Renewable Energy Laboratory, operated by Alliance for Sustainable Energy, LLC, for the U. S. Department of Energy (DOE) under Contract No. DE-AC36- 08GO28308. Funding provided by U.S. Department of Energy's Vehicle Technologies Office under the Silicon Consortium Project, directed by Brian Cunningham and managed by Anthony Burrell. The views expressed in the article do not necessarily represent the views of the DOE or the U.S. Government. The U.S. Government retains and the publisher, by accepting the article for publication, acknowledges that the U.S. Government retains a nonexclusive, paid-up, irrevocable, worldwide license to publish or reproduce the published form of this work, or allow others to do so, for U.S. Government purposes.

References

[1] K. Feng, M. Li, W. Liu, A.G. Kashkooli, X. Xiao, M. Cai, Z. Chen, Silicon-Based Anodes for Lithium-Ion Batteries: From Fundamentals to Practical Applications, Small 14 (2018). https://doi.org/10.1002/smll.201702737.

[2] Y. Orikasa, Y. Gogyo, H. Yamashige, M. Katayama, K. Chen, T. Mori, K. Yamamoto, T. Masese, Y. Inada, T. Ohta, Z. Siroma, S. Kato, H. Kinoshita, H. Arai, Z. Ogumi, Y. Uchimoto, Ionic Conduction in Lithium Ion Battery Composite Electrode Governs Cross-sectional Reaction Distribution, Scientific Reports 6 (2016) 26382. https://doi.org/10.1038/srep26382.

[3] Y. So, H.-S. Bae, Y.Y. Kang, J.Y. Chung, N.K. Park, J. Kim, H.-T. Jung, J.C. Won, M.-H. Ryou, Y.H. Kim, Eco-Friendly Water-Processable Polyimide Binders with High Adhesion to Silicon Anodes for Lithium-Ion Batteries, Nanomaterials 11 (2021) 3164. https://doi.org/10.3390/nano11123164.

[4] M. Zhang, L. Wang, H. Xu, Y. Song, X. He, Polyimides as Promising Materials for Lithium-Ion Batteries: A Review, Nanomicro Letters 15 (2023) 135. https://doi.org/10.1007/s40820-023-01104-7.
[5] J. Choi, K. Kim, J. Jeong, K.Y. Cho, M.H. Ryou, Y.M. Lee, Highly Adhesive and Soluble Copolyimide Binder: Improving the Long-Term Cycle Life of Silicon Anodes in Lithium-Ion Batteries, ACS Applied Material Interfaces 7 (2015) 14851–8. https://doi.org/10.1021/acsami.5b03364.
[6] J.S. Kim, W. Choi, K.Y. Cho, D. Byun, J. Lim, J.K. Lee, Effect of polyimide binder on electrochemical characteristics of surface-modified silicon anode for lithium ion batteries, J. Power Sources 244 (2013) 521–526. https://doi.org/10.1016/j.jpowsour.2013.02.049.
[7] J. Oh, D. Jin, K. Kim, D. Song, Y.M. Lee, M.-H. Ryou, Improving the Cycling Performance of Lithium-Ion Battery Si/Graphite Anodes Using a Soluble Polyimide Binder, ACS Omega 2 (2017) 8438–8444. https://doi.org/10.1021/acsomega.7b01365.
[8] G. Qian, L. Wang, Y. Shang, X. He, S. Tang, M. Liu, T. Li, G. Zhang, J. Wang, Polyimide Binder: A Facile Way to Improve Safety of Lithium Ion Batteries, Electrochimica Acta 187 (2016) 113–118. https://doi.org/10.1016/j.electacta.2015.11.019.
[9] M.N. Obrovac, L.J. Krause, Reversible Cycling of Crystalline Silicon Powder, J. Electrochem. Soc. 154 (2007). https://doi.org/10.1149/1.2402112.
[10] Z. Huey, Y. Ha, S. Frisco, A. Norman, G. Teeter, C.-S. Jiang, S.C. DeCaluwe, Multi-modal characterization methods of solid-electrolyte interphase in silicon-graphite composite electrodes, J. Power Sources 564 (2023). https://doi.org/10.1016/j.jpowsour.2023.232804.
[11] S. Rajendran, H. Liu, S.E. Trask, B. Key, A.N. Jansen, M.-T.F. Rodrigues, Consequences of utilizing a redox-active polymeric binder in Li-ion batteries, J. Power Sources 583 (2023). https://doi.org/10.1016/j.jpowsour.2023.233584.
[12] B.N. Wilkes, Z.L. Brown, L.J. Krause, M. Triemert, M.N. Obrovac, The Electrochemical Behavior of Polyimide Binders in Li and Na Cells, J. Electrochem. Soc. 163 (2015) A364–A372. https://doi.org/10.1149/2.0061603jes.
[13] Z. Huey, G.M. Carroll, J. Coyle, P. Walker, N.R. Neale, S. DeCaluwe, C.-S. Jiang, Impacts of Curing-Induced Phase Segregation in Silicon Nanoparticle-Based Electrodes, Submitted (2024).
[14] G. Stan, W. Price, Quantitative measurements of indentation moduli by atomic force acoustic microscopy using a dual reference method, Rev. Sci. Instrum. 77 (2006). https://doi.org/10.1063/1.2360971.
[15] X. Zhou, J. Fu, F. Li, Contact resonance force microscopy for nanomechanical characterization: Accuracy and sensitivity, J. Appl. Phys. 114 (2013).
[16] G. Stan, R.F. Cook, Mapping the elastic properties of granular Au films by contact resonance atomic force microscopy, Nanotechnology 19 (2008) 235701. https://doi.org/10.1088/0957-4484/19/23/235701.
[17] Polyimide P84NT Technical Brochure, (n.d.).
[18] TECAPOWDER PI - polyimide powder from Ensinger, (n.d.).
[19] M.R. Rosenberger, S. Chen, C.B. Prater, W.P. King, Micromechanical contact stiffness devices and application for calibrating contact resonance atomic force microscopy, Nanotechnology 28 (2017) 044003. https://doi.org/10.1088/1361-6528/28/4/044003.
[20] C. Stetson, Z. Huey, A. Downard, Z. Li, B. To, A. Zakutayev, C.S. Jiang, M.M. Al-Jassim, D.P. Finegan, S.D. Han, S.C. DeCaluwe, Three-Dimensional Mapping of Resistivity and

Microstructure of Composite Electrodes for Lithium-Ion Batteries, Nano Lett. 20 (2020) 8081–8088. https://doi.org/10.1021/acs.nanolett.0c03074.
[21] M.C. Schulze, F. Urias, N.S. Dutta, Z. Huey, J. Coyle, G. Teeter, R. Doeren, B.J. Tremolet de Villers, S.-D. Han, N.R. Neale, G.M. Carroll, Control of nanoparticle dispersion, SEI composition, and electrode morphology enables long cycle life in high silicon content nanoparticle-based composite anodes for lithium-ion batteries, J. Mater. Chem. A (2023). https://doi.org/10.1039/d2ta08935a.
[22] C. Stetson, T. Yoon, J. Coyle, W. Nemeth, M. Young, A. Norman, S. Pylypenko, C. Ban, C.-S. Jiang, M. Al-Jassim, A. Burrell, Three-dimensional electronic resistivity mapping of solid electrolyte interphase on Si anode materials, Nano Energy 55 (2019) 477–485. https://doi.org/10.1016/j.nanoen.2018.11.007.
[23] S.D. Han, K.N. Wood, C. Stetson, A.G. Norman, M.T. Brumbach, J. Coyle, Y. Xu, S.P. Harvey, G. Teeter, A. Zakutayev, A.K. Burrell, Intrinsic Properties of Individual Inorganic Silicon-Electrolyte Interphase Constituents, ACS Applied Energy Materials 11 (2019) 46993–47002. https://doi.org/10.1021/acsami.9b18252.
[24] S. Lorger, R. Usiskin, J. Maier, Transport and Charge Carrier Chemistry in Lithium Oxide, J. Electrochem. Soc. 166 (2019) A2215–A2220. https://doi.org/10.1149/2.1121910jes.
[25] C. Ma, W. Wang, Y. Chen, W. Arnold, J. Chu, Depth-sensing using AFM contact-resonance imaging and spectroscopy at the nanoscale, J. Appl. Phys. 126 (2019). https://doi.org/10.1063/1.5113567.
[26] J.P. Killgore, J.Y. Kelly, C.M. Stafford, M.J. Fasolka, D.C. Hurley, Quantitative subsurface contact resonance force microscopy of model polymer nanocomposites, Nanotechnology 22 (2011) 175706. https://doi.org/10.1088/0957-4484/22/17/175706.
[27] A.J. Heeger, Semiconducting and Metallic Polymers: The Fourth Generation of Polymeric Materials, The Journal of Physical Chemistry B 105 (2001) 8475–8491. https://doi.org/10.1021/jp011611w.
[28] C. Zhang, S. Chen, G. Zhou, Q. Hou, Y. Wang, G. Shi, A Polythiophene Material Featuring a Conjugated Carbonyl Side Group as an Anode for Lithium-Ion Batteries, ChemistrySelect 7 (2022). https://doi.org/10.1002/slct.202201699.
[29] J. Wu, X. Rui, G. Long, W. Chen, Q. Yan, Q. Zhang, Pushing Up Lithium Storage through Nanostructured Polyazaacene Analogues as Anode, Angewandte Communications 54 (2015) 7354–8. https://doi.org/10.1002/anie.201503072.
[30] T.D. Hatchard, P. Bissonnette, M.N. Obrovac, Phenolic Resin as an Inexpensive High Performance Binder for Li-Ion Battery Alloy Negative Electrodes, J. Electrochem. Soc. 163 (2016) A2035–A2039. https://doi.org/10.1149/2.1121609jes.
[31] E. Yasuda, T. Akatsu, Y. Ishiguro, L. Manocha, Y. Tanabe, Mechanical Properties of Carbon-Carbon Composites, in: B. Rand, S.P. Appleyard, M.F. Yardim (Eds.), Design and Control of Structure of Advanced Carbon Materials for Enhanced Performance, Springer, Dordrecht, 2001.
[32] J. Zhao, N. Wei, Z. Fan, J.W. Jiang, T. Rabczuk, The mechanical properties of three types of carbon allotropes, Nanotechnology 24 (2013) 095702. https://doi.org/10.1088/0957-4484/24/9/095702.
[33] Y. Zhang, W. Lv, Z. Huang, G. Zhou, Y. Deng, J. Zhang, C. Zhang, B. Hao, Q. Qi, Y.B. He, F. Kang, Q.H. Yang, An air-stable and waterproof lithium metal anode enabled by wax composite packaging, Scientific Bulletins 64 (2019) 910–917. https://doi.org/10.1016/j.scib.2019.05.025.

[34] B. Anothumakkool, F. Holtstiege, S. Wiemers-Meyer, S. Nowak, F. Schappacher, M. Winter, Electropolymerization Triggered in Situ Surface Modification of Electrode Interphases: Alleviating First-Cycle Lithium Loss in Silicon Anode Lithium-Ion Batteries, ACS Sustainable Chemistry & Engineering 8 (2020) 12788–12798. https://doi.org/10.1021/acssuschemeng.0c02391.
[35] K. Higa, V. Srinivasan, Stress and Strain in Silicon Electrode Models, J. Electrochem. Soc. 162 (2015) A1111–A1122. https://doi.org/10.1149/2.0091507jes.

In conjunction with the submission of research article entitled “Mechanical and electrical changes in electrochemically active polyimide binder for Li-ion batteries” to Journal of Materials Chemistry A, the authors declare that related data are available upon request from the corresponding author.

Corresponding author:

Chun-Sheng Jiang

National Renewable Energy Laboratory

15013 Denver West Parkway,

Golden, CO 80401, USA

Sept. 18th, 2024